

Measurement and modeling of diffuse irradiance masking on tilted planes for solar engineering applications

Daniel Tschoopp^a, Adam R. Jensen^{b,*}, Janne Dragsted^b, Philip Ohnewein^a, Simon Furbo^{b,1}

^a AEE — Institute for Sustainable Technologies, Feldgasse 19, 8200 Gleisdorf, Austria

^b Department of Civil Engineering, Technical University of Denmark, Brovej, Building 118, Kgs. Lyngby, 2800, Denmark

ARTICLE INFO

Keywords:

Solar radiation modeling
Tilted irradiance
PV
Solar thermal
View factors

ABSTRACT

Photovoltaic and solar thermal projects require accurate solar irradiance data and models for the design, assessment, and forecasting of power output. For panels and solar collectors installed in arrays, the view toward the sky and ground is restricted by the surrounding rows. This paper analyzes the impact of view obstructions on the diffuse irradiance distribution in fixed-tilt arrays, addressing the insufficient research coverage to date. Irradiance was measured using high-precision pyranometers placed at ten positions throughout an experimental solar collector array for 3.5 and 6 m row spacings and 30°, 37.5°, and 45° tilt angles (relative row spacings between 0.68 and 1.51). A novel anisotropic transposition model was developed to calculate the diffuse tilted irradiance along the collector height, accounting for diffuse irradiance masking due to view obstructions. The model was also solved inversely, obtaining local global horizontal irradiance from global tilted irradiance. The validation showed that the model accurately captures the distinct shape of the diffuse irradiance distribution. Results indicate a strong effect of view obstructions for narrow row spacings and steep tilt angles. For the most extreme configuration (3.5 m row spacing, 45° tilt angle, 1.67 relative row spacing), the diffuse irradiance was reduced to 64% at the bottom and 89% on average, relative to the top of the collector. As a consequence, measurements at the top can result in biased performance assessments.

1. Introduction

A major task in solar energy projects is the measurement and modeling of the incident solar irradiance on the collecting surfaces. The growing markets of large-scale photovoltaic and solar thermal systems pose ever higher demands on the accuracy of solar radiation data and models (Gueymard, 2014; Tschoopp et al., 2020). Errors as low as $\pm 5\%$ in solar resource calculations may jeopardize the profitability of a project (Gueymard, 2009).

Almost all flat-plate solar thermal collectors and a large share of PV panels (henceforth summarized in the term “collector”) are installed in fixed-tilt systems. Modeling the direct irradiance incident on a tilted collector surface, including self-shading in uniformly arranged arrays, involves only geometric calculations if either the Direct Horizontal Irradiance (DHI) or Direct Normal Irradiance (DNI) is known (Appelbaum and Bany, 1979). In contrast, estimation of the Diffuse Tilted Irradiance (DTI) is much more complex. For collector rows within an array, view obstructions reduce the incident diffuse radiation from the sky (an effect called *masking*) and alter reflection patterns (Appelbaum, 2018). Not only does this reduce the average diffuse irradiance,

but it also leads to a non-uniform distribution along the collector height. The parts of the collectors closest to the ground typically receive less diffuse irradiance than the upper parts. A bottom PV panel may generate 8% less power than a top panel, due solely to diffuse irradiance masking (Massalha and Appelbaum, 2020). Case studies of typical PV systems show that simple shading calculations, which only consider beam irradiance shading, underestimate shading losses by 50%–80% compared to calculations including diffuse irradiance masking (Varga and Mayer, 2021). Masking effects are also relevant for bifacial PV, which make improved use of diffuse irradiance (Gu et al., 2020). The non-uniform diffuse irradiance distribution may distort radiation measurements during the operational stage, leading to a bias in performance assessment (Ohnewein et al., 2020).

The starting point for modeling the tilted (or “plane-of-array”) irradiance in the planning phase is typically time series of Global Horizontal Irradiance (GHI). Then, following the terminology of Gueymard and Myers (2008), a *separation model* is deployed to calculate the direct and diffuse irradiance components if they are not already known. Next, a *transposition model* is applied, which predicts the transposed

* Corresponding author.

E-mail address: arajen@byg.dtu.dk (A.R. Jensen).

¹ ISES member.

Nomenclature**Latin letters**

A_i	Anisotropy index, $A_i = I_n/I_{on}$ [-]
AM	air mass [-]
BSRN	Baseline Surface Radiation Network
CC	collector array configuration for experimental setup as defined in Table 5
D_c/DTI	Diffuse Tilted Irradiance, $D_c = D_s + D_r$ [W/m ²]
D_h/DHI	Diffuse Horizontal Irradiance [W/m ²]
D_r	in-plane diffuse irradiance from reflections [W/m ²]
D_s	in-plane diffuse irradiance from the sky [W/m ²]
D_u	diffuse irradiance on ground between collectors [W/m ²]
D_v	diffuse irradiance on backside of front collector row [W/m ²]
f	shading factor [-]
$F_{X \rightarrow Y}$	view factor of surface X towards surface Y [-]
G_c/GTI	Global Tilted Irradiance, $G_c = I_c + D_c$ [W/m ²]
G_h/GHI	Global Horizontal Irradiance, $G_h = I_h + D_h$ [W/m ²]
I_c	in-plane direct irradiance, $I_c = I_n \cos \theta_c$ [W/m ²]
I_h	direct horizontal irradiance, $I_h = I_n \cos \theta_z$ [W/m ²]
I_n/DNI	Direct Normal Irradiance [W/m ²]
I_{oh}	extraterrestrial horizontal irradiance [W/m ²]
I_{on}	extraterrestrial normal incident irradiance [W/m ²]
k_T	clearness index [-]
P_x	irradiance measurement with pyranometer x [W/m ²]
R_i	transposition factor for direct radiation [-]
R_r	transposition factor for diffuse radiation from reflections [-]
R_s	transposition factor for diffuse radiation from sky [-]
%MBE	Mean Bias Error, divided by mean [%]
%RMSE	Root-Mean-Square Error, divided by mean [%]

Greek letters

β	collector tilt angle [rad]
γ	collector azimuth [rad]
δ	(absolute) collector row spacing [m]
δ_{rel}	relative collector row spacing, $\delta_{rel} = \delta/\zeta - \cos(\beta)$ [-]
Δ	sky brightness parameter, $\Delta = D_h/(AM I_{on})$ [-]
ϵ'	sky clearness parameter [-]

ζ	collector height [m]
η	collector thickness [m]
θ_c	incident angle of direct radiation on collector plane [rad]
θ_z	zenith angle [rad]
κ	collector elevation above ground [m]
λ_S	sky obstruction angle in direction of collector azimuth γ [rad]
λ_N	sky obstruction angle in opposite direction of collector azimuth γ [rad]
ρ	reflectance coefficient [-]
τ	Pearson correlation coefficient [-]
ϕ	View angle towards (obstructed) sky [rad]
ψ	View angle towards (obstructed) ground [rad]

Subscripts

avg	average
c	in-plane, collector
iso	isotropic
j	collector segment (index from $j = 1 \dots m$)
k	ground segment (index from $k = 1 \dots p$)
l	backside segment (index from $l = 1 \dots q$)
mod	modeled (predicted)
n	normal
r	reflection
s	sky
sen	sensor
u	ground
v	backside

irradiance on the tilted surface from the irradiance components. Widely used transposition models were developed by Perez et al. (1990), Hay and Davies (1980), Reindl et al. (1990), and Klucher (1979). They belong to the class of *anisotropic superposition models* (De Simón-Martín et al., 2017). The total diffuse irradiance is calculated as the sum of a background isotropic component and one or two anisotropic components representing the circumsolar region and/or horizon band.

These models are all designed for *unobstructed* tilted surfaces and only few studies are available for diffuse irradiance masking of collector arrays. For isotropic skies, modified view factors have been used by Appelbaum (2018). For anisotropic skies, Appelbaum et al. (2019)

present a modified version of the Klucher model. The most elaborate approach for collector arrays is by Varga and Mayer (2021), which propose a modified version of the Hay transposition model. Their model considers the impact of view obstructions of the front collector row separately for the isotropic and circumsolar diffuse irradiance part. The received diffuse irradiance on the collector surface from the sky is modeled similarly as proposed in this paper. However, the Varga model does not consider additional obstructions of the skyline. The calculation of reflections is only partially adjusted for the collector array setting, e.g., it assumes that the ground between the collectors receives the same diffuse irradiance as the ground in front of the first collector row and that the backside of the front collector row is non-reflective. The geometric representation and parameterization of the collector array are less detailed. Another important consideration is that all of the above-mentioned studies lack validation with measurement data.

Some simulation programs discretize view factors when obstructions are present (Anoma et al., 2017) or use average sky-view factors along the collector height, such as TRNSYS component Type 30 (Klein et al., 2009). For detailed simulations of the incident diffuse irradiance on tilted surfaces, *radiance models* describe and evaluate the radiation intensity (depending on the solid angle) over the hemisphere. Simulations for partially obstructed skies, e.g. by Ivanova and Gueymard (2019), have been developed. Other methodological approaches are *non-parametric models* like Artificial Neural Networks (ANN) (Celik and Muneer, 2013). Although these models have become increasingly integrated in solar engineering software, they are oftentimes too complex and time-consuming to apply, and only scarcely used for collector array simulations and evaluations.

During the operating phase of large-scale systems, Global Tilted Irradiance (GTI) is typically measured for monitoring or control purposes (Bava and Furbo, 2018). Many solar plants do not measure GHI,

even though this can be done at a relatively low cost. The data gap can be filled with the calculation of GHI from GTI by inverting separation and transposition models. This so-called *inverse* direction has been much less investigated than the *forward* direction (Yang et al., 2013; Housmans and Bertrand, 2017). The importance of the *inverse* direction is due to the fact, that local GHI data is necessary for endogenous time-series models for solar radiation (Voyant et al., 2017) and many nowcasting and forecasting models for PV power generation (Sobri et al., 2018). Solving the inverse problem also allows calculating DNI from GTI. Once DNI is known, self-shading of the collector array from direct radiation can be calculated for improved model-based control or in-situ performance assessment (Ohnewein et al., 2020).

The novelty of this paper lies in three areas. First, an analysis of a new solar radiation data set, which includes multiple high-precision pyranometer measurements along the collector height, is presented for six array configurations. The existence of comparable data sets is not known to the authors. It is provided as supplementary material for free download. Second, a modified version of the anisotropic Hay-and-Davies transposition model is developed which considers view obstructions in fixed-tilt collector arrays. Third, this model is also applied in the inverse direction. The model structure is deliberately kept parsimonious to allow a straightforward application in solar engineering practice.

The structure of this paper is as follows: The model development and formulation are described in Section 2. The experimental collector array and measurement instrumentation are presented in Section 3. The experimental data analysis and model validation are performed in Section 4. The conclusion is presented in Section 5.

2. Model

Before applying transposition models, a separation model is deployed if the direct and diffuse irradiance components are not known. In this study, the Erbs separation model is used (Erbs et al., 1982). The model is chosen due to its good performance and simple mathematical structure (Gueymard, 2009), which is helpful when solving the inverse problem. The novel anisotropic transposition model developed in this paper builds on the Hay-and-Davies model (Hay and Davies, 1980), henceforth called the Hay model. This section describes the original Hay transposition model, its limitations for collector arrays, and the novel transposition model.

2.1. Erbs separation model

The Erbs separation model is based on the clearness index:

$$k_T = \frac{G_h}{I_{oh}} \quad (1)$$

where G_h is the global horizontal irradiance and I_{oh} is the extraterrestrial horizontal irradiance. The Erbs separation model then calculates the diffuse share as:

$$\frac{D_h}{G_h} = \begin{cases} 1.0 - 0.09 k_T & \text{if } k_T \leq 0.22 \\ 0.9511 - 0.1604 k_T + 4.388 k_T^2 & \text{if } 0.22 < k_T \leq 0.8 \\ -16.638 k_T^3 + 12.336 k_T^4 & \text{if } 0.8 < k_T \leq 0.9 \\ 0.165 & \text{if } k_T > 0.9 \end{cases} \quad (2)$$

where D_h is the diffuse horizontal irradiance.

2.2. Original Hay transposition model and its limitations

The Hay model calculates the transposed global tilted irradiance, G_c , with the following equation:

$$G_c = I_c + D_s + D_r \quad (3)$$

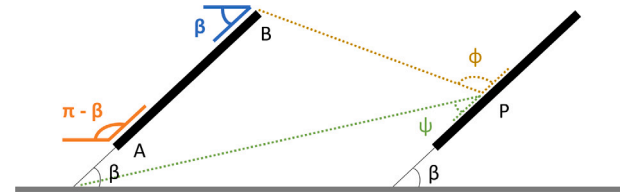


Fig. 1. Illustration of view factors.

where I_c is in-plane direct irradiance, D_s is in-plane diffuse irradiance from the sky, and D_r is in-plane diffuse irradiance from reflections. The components are calculated as follows:

$$I_c = I_h R_i \quad (4)$$

$$D_s = D_h ((1 - A_i) R_d + A_i R_i) \quad (5)$$

$$D_r = \rho G_h R_r \quad (6)$$

R_i , R_d , and R_r are the transposition factors for the direct horizontal irradiance, I_h , diffuse horizontal irradiance, D_h , and global horizontal irradiance, G_h , respectively. ρ is the reflectance coefficient of the ground. A_i is the anisotropy index. R_i can be calculated by simple geometric relations:

$$R_i = \frac{I_c}{I_h} = \frac{I_n \cos \theta_c}{I_n \cos \theta_z} \quad (7)$$

Formulas to calculate the angles of incidence on the collector, θ_c , and solar zenith angle, θ_z , can be found in standard texts, e.g., Duffie et al. (2020). The geometric idea leading to the transposition factors R_d and R_r can be seen in the first (left) collector row of Fig. 1.

R_d is equal to the sky view factor of angle $\pi - \beta$ (for isotropic sky):

$$R_d = \frac{1 - \cos(\pi - \beta)}{2} \quad (8)$$

Similarly, R_r is given by the view factor of angle β towards the ground:

$$R_r = \frac{1 - \cos \beta}{2} \quad (9)$$

The anisotropy index A_i is a function of the transmittance of the atmosphere for direct radiation:

$$A_i = \frac{I_h}{I_{oh}} = \frac{I_n \cos \theta_z}{I_{on} \cos \theta_z} \quad (10)$$

The model assumes that the horizon extends infinitely in front of the collector with no interfering mask and a uniform reflectance coefficient, ρ , for the ground. The modeled irradiance is the same at all points from A to B along the collector height. For the second row, the view is partially obstructed, as shown for point P in Fig. 1. Accordingly, the view angles towards the sky ϕ and towards the ground ψ differ from $\pi - \beta$ and β , respectively, and vary along the collector height. Thus, the transposition factors in Eq. (8) and (9) are no longer valid. The incident irradiance on the ground between the collector is not equal to G_h as Eq. (6) implies and some parts of the collector may be shaded. For these reasons, the Hay model cannot be directly applied to collector arrays with obstructed views.

The Hay model is generally characterized by its high accuracy as shown by comparative studies by Gueymard (2009), Yang (2016) and Noorian et al. (2008). It considers the diffuse brightening of the circumsolar region as an additional radiation component concentrated at the position of the sun, treating it with the same transposition factor, R_i , as the direct radiation. This simplifies the circumsolar radiance (Blanc et al., 2014) and lowers the model accuracy when the sun is hidden behind an object, but close to the edge, where the circumsolar radiance is not fully blocked. How problematic this issue

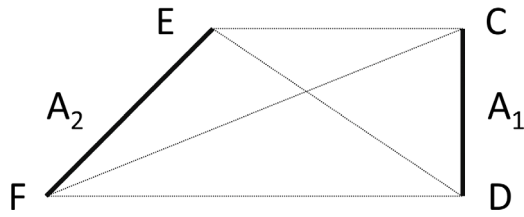


Fig. 6. Hottel crossed-string rule.

The collector, ground, and backside are split into segments. Each collector segment j , ground segment k , and backside segment l is assigned a reflectance coefficient: $\rho_{c,j}$, $\rho_{u,k}$, and $\rho_{v,l}$, respectively. The number of segments can be chosen according to the desired precision and resolution.

View factors

The model uses view factors to calculate the radiation exchange between surfaces (or the sky) that emit isotropic diffuse radiation, i.e., have the same radiant intensity in every direction. For two surfaces, A_1 and A_2 , the view factor from A_1 to A_2 is denoted by $F_{1 \rightarrow 2}$ and is defined as:

$$F_{1 \rightarrow 2} = \frac{\text{diffuse radiation leaving } A_1, \text{ incident on } A_2}{\text{total diffuse radiation leaving } A_1} \quad (11)$$

A convenient formula to calculate the view factor between two surfaces of infinite length (for example, view factor $F_{u,k \rightarrow v,l}$ between ground segment k and backside segment l in Fig. 5) is given by the “Hottel crossed-string rule” (Hottel and Sarofim, 1967). Using the nomenclature depicted in Fig. 6, the view factor can be calculated as follows:

$$F_{1 \rightarrow 2} = \frac{CF + DE - CE - DF}{2 \cdot CD} \quad (12)$$

The derivation of the view factor calculation between any segment and the (obstructed) sky can be found in Robinson and Stone (2004) and Maor and Appelbaum (2012). In particular, for any segment located at point P on the collector with view angle ϕ , as shown in Fig. 1, the view factor is determined as follows:

$$F_{P \rightarrow s} = \frac{1 - \cos(\phi)}{2} \quad (13)$$

Sky irradiance

In the calculation process, the first step is to calculate the incident irradiance from the sky for each segment. The direct irradiance, $I_{c,j}$, on a collector segment, j , is given by:

$$I_{c,j} = I_c f_j \quad (14)$$

where I_c is calculated from Eq. (4). The shading factor, f_j , is defined as:

$$f_j = \begin{cases} 1 & \text{if collector segment } j \text{ is unshaded} \\ 0 & \text{otherwise} \end{cases} \quad (15)$$

An analytical formula for the shadow height on a collector can be found in Bany and Appelbaum (1987). Similarly, the direct irradiance, $I_{u,k}$, on a ground segment, k , is given by:

$$I_{u,k} = I_n \cos \theta_z f_k = I_h f_k \quad (16)$$

where $f_k = 1$ if the ground segment is unshaded.

The diffuse irradiance from the sky on collector segment j is calculated as follows:

$$D_{s,j} = D_h ((1 - A_i)F_{j \rightarrow s} + A_i R_i f_j) \quad (17)$$

where D_h , A_i and R_i are defined as in the original Hay model (see Section 2.2). $F_{j \rightarrow s}$ is the view factor of segment j towards the sky (see Eq. (13)).

The calculation of the diffuse irradiance from the sky on a ground or backside segment follows the same structure as Eq. (17), with the respective view, transposition, and shading factors.

Reflections

Reflections are assumed to be the same for each angle (Lambertian reflection). This assumption, although never completely accurate, is widely used in solar engineering (Gueymard et al., 2019).

For each collector, ground, or backside segment, n , the reflected irradiance,

$$G_{r,n} = \rho_n G_{inc,n} \quad (18)$$

is a fraction of the incident irradiance $G_{inc,n}$, depending on the reflectance coefficient, ρ_n , of the surface. The incident irradiance on surface segment x can be calculated as follows:

$$G_{inc,x} = I_x + D_x + \sum_n F_{x \rightarrow n} G_{r,n} \quad (19)$$

where I_x and D_x denote the direct and diffuse irradiance received from the sky. The last term is the contribution of all surfaces, n , that are viewed from surface x with view factor $F_{x \rightarrow n}$, e.g., all ground and backside segments if x is a collector segment.

Substituting Eq. (18) into Eq. (19) yields a system of $(m + p + q)$ equations, which can be solved for the incident irradiance:

$$\vec{G}_{inc} = (I - FR)^{-1} \cdot (\vec{I} + \vec{D}) \quad (20)$$

where I is the identity matrix, F the view factor matrix, and R the reflectance matrix. The explicit form of the matrix, to ease the implementation, can be found in Appendix A. By default, reflectance coefficients of the collector segments are set to zero.

Inverse application

The inverse application of the Hay-C model (case (C) and (D) in Table 1) only works if, for each measured value of $G_{c,sen}$, the horizontal irradiance, G_h , that solves the forward model is unique. In other words, the forward model, denoted by H , must be a strictly increasing function, i.e.:

$$\frac{dG_{c,sen}}{dG_h} = \frac{dH(G_h)}{dG_h} > 0 \quad (21)$$

within the valid range of G_h . For case (D), the model is invertible, as I_h is fixed, and an increase in G_h increases D_h , which leads to an increase in $G_{c,sen}$. For case (C), however, the model might not be invertible. An increase in G_h increases k_T , which implies that the direct horizontal irradiance share D_h/G_h decreases or remains constant (see Eq. (1) and (2)). Therefore I_h increases, but D_h may decrease. If the ratio of the transposition factor for direct radiation to the sky view factor of the sensor, $R_i/F_{sen \rightarrow s} \geq 1$, then the model is invertible regardless of other conditions. But if this ratio is strictly smaller than 1, higher levels in G_h may not necessarily increase $G_{c,sen}$. $F_{sen \rightarrow s}$ depends only on the collector array geometry and is constant. R_i is small when the incidence angle on the collector, θ_c , is substantially greater than the zenith angle, θ_z (see Eq. (7)). Thus, invertibility problems typically occur just after the sun appears in front of the collector or disappears behind the collector with incidence angle θ_c reaching $\pi/2$. Conditions, where the inverse solution does not exist make up a small portion of radiation conditions. For the filtering criteria of the radiation experiments (see Section 3.3), the model was invertible for all recorded data points.

Implementation

The model was implemented in ADA, an object-oriented data analysis and simulation tool for renewable energy applications based on MATLAB® developed by AEE INTEC (Ohnewein et al., 2017). The inverse model is solved with an array solver using the fast and robust bisection method as recommended by Yang et al. (2013) with the code provided by Sartorius (2020). Typical yearly simulation runs with data in 1 min resolution take around 30 s on a computer with a dual-core CPU and 2.5 GHz CPU frequency.

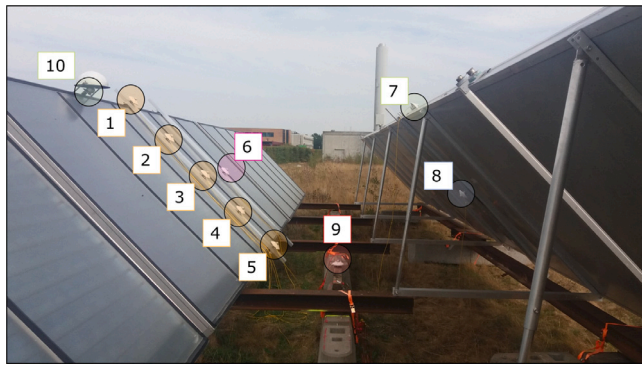


Fig. 7. Experimental setup consisting of six flat-plate solar collectors and ten pyranometers (numbered).

Table 2
Collector dimensions and positions.

Parameter	Value	Unit
Collector area	15.0	m ²
Collector width	5960	mm
Collector height (ζ)	2520	mm
Collector thickness (η)	124	mm
Elevation above ground (κ)	626	mm

3. In situ measurements

3.1. Experimental collector array

The experimental setup consisted of two rows of three collectors, thus the rear middle collector experienced approximately the same irradiance conditions as any non-perimeter collector in an array. The irradiance distribution in the experimental array was measured using ten high-precision pyranometers, as shown in Fig. 7.

The setup was located on an even grass field on the campus of the Technical University of Denmark (DTU) in Kgs. Lyngby, near Copenhagen (latitude 55.793° N, longitude 12.524° E, elevation 36 m). The location has a typical coastal climate, strongly influenced by its proximity to both the sea and the European continent, with yearly global horizontal irradiation levels of around 1,050 kWh/m². Summers have cool and changeable weather with substantial cloud cover (Laursen et al., 1999).

Each of the six collectors was propped up with two adjustable aluminum poles, which made it possible to adjust the collector tilts. The second row of collectors was placed on I-beams, along which the collectors could slide, allowing for the row spacing to be changed. The collectors were Sunmark flat-plate collectors, which are used for large-scale solar thermal plants. The collector dimensions are summarized in Table 2. The collectors were kept south-oriented during the entire measurement period. The backside of the collectors was unpolished aluminum with an assumed reflectance coefficient of $\rho_v = 0.8$ (Ayieko et al., 2015). A reflectance coefficient of $\rho_u = 0.2$ was assumed for all ground segments due to the lack of measurement.

Toward the south, 90 m from the experimental array, dense trees formed a line parallel to the east–west axis of the array, obstructing the view towards the horizon. The height of the trees (14 m) was determined with an altimeter on a drone. The resulting sky obstruction angle in the direction of the collector azimuth was $\lambda_S = 9.0^\circ$. Towards the north, there were no view obstructions ($\lambda_N = 0^\circ$).

Pyranometers 1–5 were used to measure the irradiance distribution along the collector height and were therefore positioned with an even spacing along the center of the rear middle collector. Pyranometer 6 was offset to the side of 1–5 and repositioned during the experimental period for comparison purposes. Similar to pyranometer 1, pyranometer 7 was placed on the collector in the front row. Pyranometer 8

Table 3

Pyranometer and pyrliometer uncertainty contributions at 95% confidence ($k = 2$). 'Worst case' values stated by manufacturer (Kipp & Zonen, 2016, 2019).

	Pyranometer CMP11	Pyrliometer CHP1
Zero offset A	< 7 W/m ²	–
Zero offset B	< 2 W/m ²	< 1 W/m ²
Non-stability	< 0.5%	< 0.5%
Non-linearity	< 0.2%	< 0.2%
Directional response	< ± 10 W/m ²	–
Temperature response	< 1%	< 0.5%
Spectral response	< 3%	< 1%
Tilt response	< 0.2%	–

was placed in the center of the backside of the front middle collector. Pyranometer 9 was placed between the two collector rows horizontally. Pyranometer 10 was offset from pyranometer 1 and shaded by a half-dome that covered the pyranometer's view to the sky. This was done to investigate the reflected radiation from the ground and backside of the front collector row. Since all pyranometers, except for 9, were mounted in the collector plane, they changed tilt according to the adjusted tilt of the collectors.

All sensors were Kipp & Zonen (K&Z) CMP11 thermopile pyranometers. The measurements were logged with a 10-channel Hioki LR8431 data logger with a 1-second resolution. Due to the extended time frame of the experiment, the data logger accumulated a time drift of two minutes during the measurement period. This was compensated for by recording the time offset every time the pyranometers were cleaned and applying a linear correction for the time drift afterward.

3.2. DTU climate station

Measurements of global, diffuse, and direct normal irradiance were obtained from the Climate Station at DTU, located 250 m from the experimental collector array. The DTU Climate Station includes a permanently installed solar tracker with instruments for measuring GHI, DHI, and DNI (Andersen et al., 2017). The solar tracker is located on the rooftop of a building belonging to the university and continuous measurements have been made since 1990. Direct normal irradiance is measured with a K&Z CHP1 pyrliometer (half opening angle of 2.5°). Diffuse horizontal irradiance is measured with a K&Z CMP11 pyranometer shaded by a shadow ball (view angle of 5°). Global horizontal irradiance is also measured with a K&Z CMP11 pyranometer. All three instruments are mounted on the same K&Z SOLYS 2 tracker. Measurements are logged with a 1-min resolution. As global irradiance can be more accurately calculated from the diffuse and direct components, the GHI measurements were only used for quality control (Gueymard and Myers, 2009).

3.3. Measurement uncertainty and data filtering

All measurement instruments used in this study are thermopile sensors, which have an optically black surface that increases in temperature according to the incident irradiance. The irradiance is calculated from the temperature difference between the black surface and the instrument body. This indirect measurement method is associated with several uncertainty sources (see Table 3).

Another consideration to take into account is the time frame of interest, e.g., instantaneous values, integrated hourly, or daily totals. For DNI measurements made with a good quality pyrliometer, such as the one mounted on the tracker, it is possible to achieve minute, hourly, and daily uncertainty levels of 1.8%, 1.5%, and 1.0%, respectively. Similarly, the achievable uncertainty levels for pyranometers measuring hourly and daily totals of GHI are 3% and 2%, respectively (World Meteorological Organization, 2017).

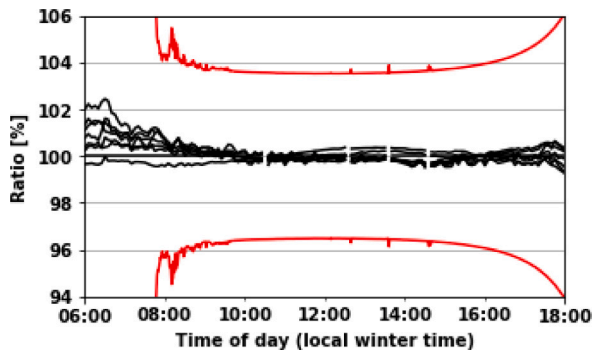


Fig. 8. Irradiance measurement of pyranometers 2–9, relative to pyranometer 1, during one day of the calibration process (black lines). Worst-case uncertainty based on Table 3 (red lines). (For interpretation of the references to color in this figure legend, the reader is referred to the web version of this article.)

Most solar radiation models predict a single irradiance value in W/m^2 , hence the uncertainty of the absolute measurement is of interest. However, a primary output from the Hay-C model is the prediction of the irradiance along the collector height relative to the top of the collector (pyranometer 1) in %. The “relative measurement” for pyranometers 2–5 can be defined as $(G(P_x) - G(P_1))/G(P_1)$. In order to estimate the uncertainty of the relative measurement, all pyranometers were installed horizontally adjacent to each other on the DTU Climate Station platform for a joint calibration. As the pyranometers were all mounted identically and exposed to the same conditions, they should ideally measure the same value. Measurements were taken for a 5-day period. The uncertainty for the relative measurement was then estimated based on the deviation between the pyranometers, calculated as the standard deviation multiplied by a coverage factor ($k = 2$), according to the GUM method (Joint Committee for Guides in Metrology, 2008). The expanded uncertainties for the relative pyranometer measurements ranged from $\pm 0.9\%$ to $\pm 1.8\%$, with a mean of $\pm 1.2\%$. The relative measurements for one day during the calibration process are shown in Fig. 8. For comparison, the worst-case uncertainty from Table 3 has also been plotted in the figure and, as expected, the deviation of the relative measurements was significantly lower than the absolute measurement uncertainty.

All instruments at the experimental field and DTU Climate Station were inspected and cleaned weekly to limit the effect of soiling, with only a few exceptions. For the validation, data were averaged for each 5 min. The filtering criteria used to derive the validation data set are listed in Table 4. These criteria entail quality checks, as recommended by the BSRN network (Long and Dutton, 2010). The restrictions regarding minimum global horizontal and global tilted irradiance and maximum beam incident angle aim to remove data with larger uncertainty. Periods with shading are excluded from the validation, as this would add additional uncertainties.

The diffuse in-plane irradiance along the collector height, $D_c(P_x)$, is calculated as the difference of the measured global tilted irradiance, $G_c(P_x)$, minus the calculated in-plane direct irradiance, I_c , from DNI measurements. As DNI is measured at the DTU Climate Station 250 m from the experimental setup, the radiation conditions might differ between the two locations. Averaging the data to 5 min and selecting only data with a diffuse share between 0 and 1 reduces these inconsistencies.

3.4. Experiments

Experiments were conducted from August 2018 to May 2020. Measurements were made for two row spacings (3.5 m and 6 m) and three tilt angles (30° , 37.5° , and 45°), leading to six collector array configurations (CC), as shown in Table 5. All-sky conditions were used to obtain the validation data set for each setup, only discarding data that did not meet the filtering criteria. The requirement to have no shading led to the exclusion of most of the data from the winter periods.

Table 4

Validation data filtering criteria.

Limits				
50 W/m ²	≤	$D_h + I_h$	≤	$1.2 I_{on} \cos(\theta_z)^{1.2} + 50 \text{ W/m}^2$
0 W/m ²	≤	I_n	≤	$0.95 I_{on} \cos(\theta_z)^{0.2} + 10 \text{ W/m}^2$
0 W/m ²	≤	D_h	≤	$0.75 I_{on} \cos(\theta_z)^{1.2} + 30 \text{ W/m}^2$
50 W/m ²	≤	$G_c(P_x)$	≤	$1.2 I_{on} \cos(\theta_c)^{1.2} + 50 \text{ W/m}^2$
Comparison				
0.92	≤	$G_h/(D_h + I_h) \leq 1.08$		
Beam incidence angle				
θ_z	≤	80°		
θ_c	≤	80°		
Diffuse irradiance share				
0	≤	$D_h/(D_h + I_h) \leq 1$		
0	≤	$(G_c(P_x) - I_c)/G_c(P_x) \leq 1$		
Shading				
No internal shading (formulas by Appelbaum and Bany (1979))				
No external shading ($\lambda_s = 9.0^\circ$)				

Table 5

Investigated collector array configurations (CC) and time periods with valid data. The relative row spacing is the ratio of the row distance minus the horizontal projection of the front collector to the collector height.

CC #	Row spacing δ	Tilt β	Relative row spacing δ_{rel}	Time period
1	3.5 m	45.0°	0.68	Aug. 2018
2	3.5 m	37.5°	0.60	Mar. - May 2019
3	3.5 m	30.0°	0.57	Aug. - Sep. 2018
4	6.0 m	45.0°	1.67	Jul. 2019
5	6.0 m	37.5°	1.59	May - Jul. 2019
6	6.0 m	30.0°	1.51	Mar. - May 2020

4. Experimental data analysis and model validation

4.1. Experimental data analysis

Fig. 9 illustrates measurement results of the diffuse radiation distribution within one collector array (configuration CC #1) and the DTU Climate Station. Measurements at the top of the back row, $D_c(P_1)$, and the top of the front row, $D_c(P_7)$, were highly correlated ($r = 0.998$ for CC #1, and between 0.996 and 0.999 for the other setups). Mean values for $D_c(P_7)$ were slightly higher, due to higher reflections (+2.3% for CC #1, between +1.8% and +4.0% for other setups). D_h lies in a similar range as $D_c(P_1)$ (+1.6% for CC #1, between −7.5% and +6.7% for other setups). The obstructed sky view of sensor P_1 , when compared to D_h , decreases the diffuse irradiance for isotropic conditions. However, for anisotropic conditions, the irradiance can be higher since the sensor is tilted.

While $D_u(P_9)$ is aligned horizontally, it is substantially lower than D_h , as the sensor does not see the whole hemisphere (−43.8% for CC #1, between −49.6% and −45.6% for other setups). Diffuse irradiance on the backside of the collector, $D_c(P_8)$, was 37.8 W/m^2 on average for CC #1 and between 16.4 W/m^2 and 53.3 W/m^2 for the other setups. $D_c(P_{10})$ had one-digit mean values close to zero (4.0 W/m^2 for CC #1, between 1.9 W/m^2 and 5.1 W/m^2 for other setups). Note that the reported values give some indication of irradiance differences in various spots in a collector array, but should not be overinterpreted, as the radiation experiments were conducted during different times of the year and only data fulfilling the filtering criteria were used. The validity of the model for 3D effects on the collector plane, i.e., irradiance differences in the east–west direction, was not the focus of the radiation experiments. However, various placements of sensor P_6 in the collector plane, shifted both in the east–west direction and along the collector height, showed that there was no significant difference between the measurements of sensor P_6 and the respective sensor P_1 to P_5 placed at the same height.

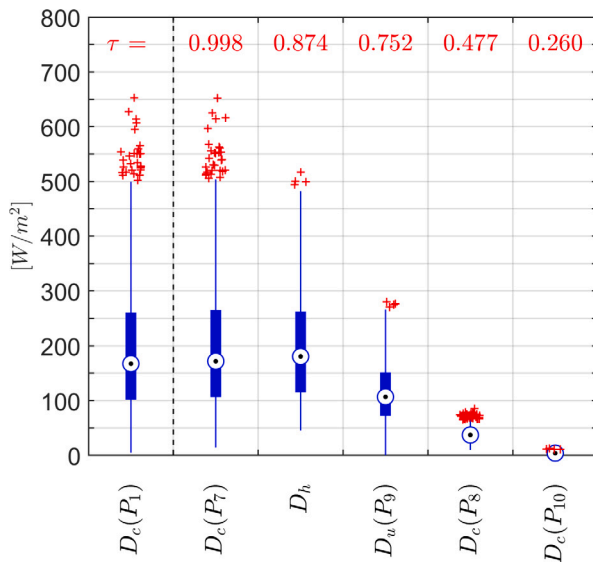


Fig. 9. Box plot of diffuse irradiance at different locations in the collector array for configuration CC #1 and the DTU Climate Station. Red markers are outliers, τ is the Pearson correlation coefficient with respect to $D_c(P_1)$. (For interpretation of the references to color in this figure legend, the reader is referred to the web version of this article.)

Fig. 10 shows the diffuse and global irradiance for all sensors normalized to P_1 (top sensor) (= 100%) for all configurations. For the narrow row spacing (CC #1-3), the diffuse irradiance reduction is substantial, dropping as low as 64% for sensor P_5 in CC #1, whereas, for the wide row spacing (CC #4-6), the effect is marginal. Note that the diffuse irradiance levels for sensors P_1 and P_2 are very similar for all configurations. This is an indication of the obstructed horizon towards the south, which made sensors P_1 and P_2 receive essentially the same irradiance from the sky. Also note that P_3 measures higher diffuse irradiance levels than P_1 for CC #4-6. This atypical behavior can occur due to increased reflections, which overcompensates for the reduced sky view.

The reduction of global irradiance is less extreme, as all sensors receive the same direct irradiance. The trend of global irradiance reduction is similar to that of the diffuse irradiance reduction, but exposes some differences, as the diffuse shares of the global irradiance vary among the setups (see Table 6 for irradiance levels of the experiments).

The red lines indicate the average irradiance over the collector for each configuration. They are calculated by integration of the linearly interpolated measurement values of sensors P_1 to P_5 along the collector height and subsequent division by the collector height:

$$Irr_{c,avg} = \frac{1}{4} \sum_{x=1}^4 \frac{Irr(P_x) + Irr(P_{x+1})}{2} \quad (22)$$

where Irr is either diffuse or global irradiance. For the narrow row spacing (CC #1-3), the average diffuse irradiance is substantially reduced (down to 89 % for CC #1), whereas, for the wide row spacing (CC #4-6), the reduction is 1-2 % for all configurations.

A more detailed analysis of the diffuse irradiance reduction is shown in Fig. 11, which displays the diffuse irradiance measured by sensors P_2 - P_5 vs. the top sensor, P_1 , for four configurations. The figure shows that the diffuse irradiance toward the bottom is not only lower but that the scatter significantly increases. This is most likely due to a partial blocking of the circumsolar irradiance when the sun is close to the edges, an issue that will be analyzed in Section 4.2.

4.2. Overall statistical results for model validation

For the model validation, the number of collector segments was $m = 500$, ground segments $p = 20$, and backside segments $q = 20$.

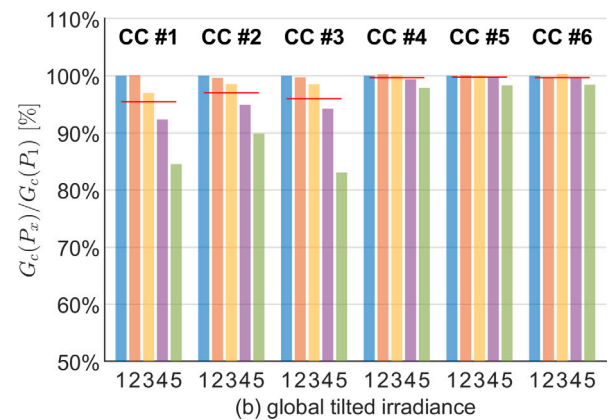
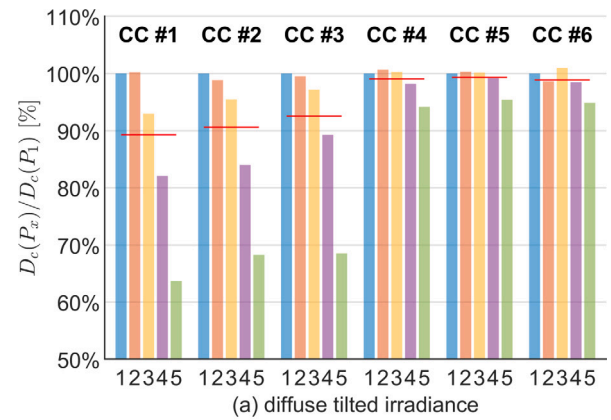


Fig. 10. Irradiance distribution for (a) diffuse tilted irradiance and (b) global tilted irradiance along the collector height relative to the top sensor ($P_1 = 100\%$). Numbers 1 to 5 refer to sensors P_1 to P_5 . Red lines indicate averages among the five sensors. (For interpretation of the references to color in this figure legend, the reader is referred to the web version of this article.)

Relative Mean Bias Error (%MBE) and relative Root Mean Square Error (%RMSE) are used as error metrics

$$\%MBE = \frac{\frac{1}{n} \sum (\widehat{Irr} - Irr)}{\frac{1}{n} \sum Irr} \quad [\%] \quad (23)$$

$$\%RMSE = \frac{\sqrt{\frac{1}{n} \sum (\widehat{Irr} - Irr)^2}}{\frac{1}{n} \sum Irr} \quad [\%] \quad (24)$$

where \widehat{Irr} is the modeled and Irr is the measured irradiance.

Table 6 shows the model accuracy for all collector array configurations and calculation cases, a total of 24 scenarios. For the two forward cases, (A) and (B), the model tends to underestimate the global tilted irradiance at the top, $G_c(P_1)$. In case (A), the Erbs model overestimates the direct horizontal irradiance, underestimates the diffuse horizontal irradiance, and transposes this pattern to the tilted surface. In case (B), the diffuse tilted irradiance at the top is also underestimated, but to a lesser degree. For the inverse direction, cases (C) and (D), the model overestimates the global horizontal irradiance with a bias similar in magnitude to the forward direction, but opposite in sign. This modeling feature, assuming no invertibility problems occur, should be expected, as the governing system of equations for the radiation transposition are simply reversed. The inverse direction shows reasonable accuracy, including the split of the global irradiance in its direct and diffuse parts. For the prediction of the global tilted irradiance, the modeling bias for the direct tilted irradiance (overestimation) and the diffuse tilted irradiance (underestimation) partially cancel out for cases (A) and (C). This can result in a lower bias for the global tilted irradiance than

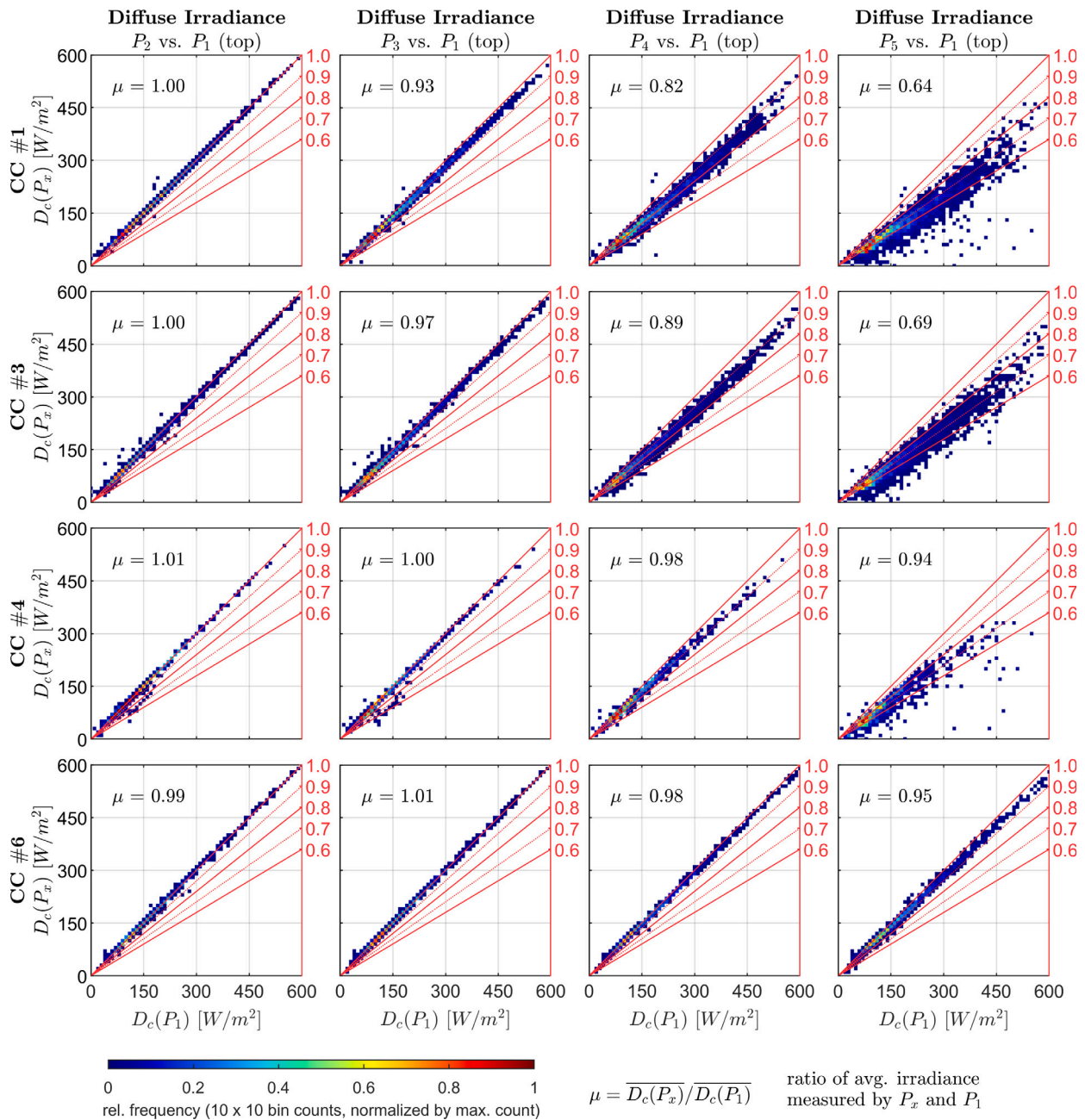


Fig. 11. Measured diffuse irradiance on top and along the collector height for four configurations. (For interpretation of the references to color in this figure legend, the reader is referred to the web version of this article.)

for cases (B) and (D) where the direct radiation is measured, although %RMSE are typically higher, as is to be expected.

The global tilted and diffuse tilted irradiance, $G_{c,avg}$ and $D_{c,avg}$ (as defined in Eq. (22)), show less underestimation or a shift to slight overestimation. For all cases, the prediction of the average global tilted irradiance shows good agreement with the measurements. %RMSE are substantially higher for the direct and diffuse radiation components than for their sum. Modeling errors for the top sensor and the average over the sensors are similar, indicating that they mainly stem from the horizontal to tilted transposition and radiation separation, and not from the irradiance distribution along the collector height. This is also confirmed by very low %RMSE for case (D), where $G_{c,sen}$ is measured.

Reasons for the relatively high %RMSE values can lie in the extremely changeable weather conditions at the site, for which the prediction accuracy of radiation models is known to be lower (Gueymard, 2009), especially for the high sample rate of 5 min. The difference

between irradiance conditions at the experimental collector array and that for the DTU Climate Station may also increase %RMSE. Another possible error source is that the line of trees forming the horizon does not completely block the diffuse radiation from the sky. Inaccurate assumptions or modeling errors regarding reflections likely do not have a large effect on the overall predicted diffuse tilted irradiance on top of the collector, as low recorded values of sensor P_{10} indicate (see Section 4.1).

4.3. Errors pertaining to radiation separation

Additional evaluations are presented for a better assessment of the model performance when using the Erbs separation model. For configuration CC #1, case (A), Fig. 12 shows the diffuse fraction vs. clearness index for the measurement data and the Erbs correlation.

Table 6

Model performance for all collector array configurations (see Table 5) and calculation cases (see Table 1). Empty cells correspond to measured input values.

Setup/Case	%MBE [%]								%RMSE [%]							
	G_h	I_h	D_h	$G_c(P_1)$	I_c	$D_c(P_1)$	$G_{c,avg}$	$D_{c,avg}$	G_h	I_h	D_h	$G_c(P_1)$	I_c	$D_c(P_1)$	$G_{c,avg}$	$D_{c,avg}$
CC #1 ($\delta = 3.5$ m, $\beta = 45^\circ$, $\delta_{rel} = 0.68$)																
Reference [W/m ²] ($N = 2737$, 228.1 h)	415	218	196	453	260	193	433	173								
(A) - forward			5.42	-6.02	-2.53	6.19	-14.26	-0.50	-10.59	31.16	34.64	14.13	32.13	41.88	15.20	42.01
(B) - forward				-3.97			-9.32	-2.25	-5.63			12.91		30.28	12.87	32.27
(C) - inverse	2.00	9.98	-6.88		10.76	-14.48	2.22	-10.65		10.45	31.67	32.35	32.57	43.83	3.42	43.94
(D) - inverse	5.08		10.73				1.56	3.92		15.76		33.27			2.68	6.72
CC #2 ($\delta = 3.5$ m, $\beta = 37.5^\circ$, $\delta_{rel} = 0.60$)																
Reference [W/m ²] ($N = 4605$, 383.8 h)	436	277	158	506	344	162	491	146								
(A) - forward			1.90	-3.33	-1.38	1.90	-8.35	0.16	-3.93	21.43	37.53	9.45	21.39	43.94	10.02	45.34
(B) - forward				-1.99			-6.24	-0.59	-1.99			8.82		27.61	8.89	29.78
(C) - inverse	1.25	4.23	-3.97		4.08	-8.70	1.60	-4.22		7.77	21.99	36.51	21.67	46.15	2.45	47.45
(D) - inverse	2.63		7.25				1.31	4.41		10.90		29.99			2.14	7.18
CC #3 ($\delta = 3.5$ m, $\beta = 30^\circ$, $\delta_{rel} = 0.57$)																
Reference [W/m ²] ($N = 861$, 71.8 h)	237	92	146	263	121	141	252	131								
(A) - forward			1.01	-0.64	-0.40	1.62	-2.13	1.16	0.74	47.53	29.99	11.59	48.55	37.30	12.54	38.34
(B) - forward				-1.38			-2.56	0.05	0.09			10.99		20.43	11.17	21.54
(C) - inverse	0.42	0.71	0.24		1.37	-1.15	1.57	1.76		7.96	43.19	28.23	43.97	37.77	3.63	39.00
(D) - inverse	1.92		3.13				1.37	2.63		12.52		20.42			3.30	6.36
CC #4 ($\delta = 6$ m, $\beta = 45^\circ$, $\delta_{rel} = 1.67$)																
Reference [W/m ²] ($N = 1571$, 130.9 h)	526	318	208	537	342	195	535	193								
(A) - forward			5.43	-8.32	-0.80	5.67	-12.18	-0.50	-11.44	23.40	35.87	11.98	24.02	42.16	12.11	42.01
(B) - forward				-1.83			-5.04	-1.58	-4.40			11.29		31.15	11.34	31.47
(C) - inverse	0.60	6.78	-8.88		7.13	-12.56	0.31	-11.80		9.67	25.67	34.12	26.13	45.95	0.66	45.69
(D) - inverse	2.24		5.68				0.22	0.60		12.95		32.81			0.58	1.61
CC #5 ($\delta = 6$ m, $\beta = 37.5^\circ$, $\delta_{rel} = 1.59$)																
Reference [W/m ²] ($N = 3982$, 331.8 h)	533	325	208	567	359	208	565	207								
(A) - forward			4.97	-7.80	-1.82	5.19	-13.93	-1.63	-13.49	23.07	36.17	12.38	23.61	43.08	12.42	42.98
(B) - forward				-2.66			-7.26	-2.52	-6.89			11.72		31.95	11.71	32.06
(C) - inverse	1.60	8.34	-8.98		8.54	-14.74	0.20	-14.28		10.15	26.82	34.88	27.33	47.18	0.46	46.98
(D) - inverse	3.19		8.20				0.13	0.35		13.40		34.40			0.42	1.16
CC #6 ($\delta_{abs} = 6$ m, $\beta = 30^\circ$, $\delta_{rel} = 1.51$)																
Reference [W/m ²] ($N = 3308$, 275.7 h)	408	268	140	495	343	152	493	150								
(A) - forward			0.06	-0.12	-1.80	0.12	-6.12	-1.51	-5.22	20.81	39.64	10.44	20.67	47.15	10.40	47.55
(B) - forward				-2.20			-7.16	-1.92	-6.29			9.98		32.49	9.94	32.61
(C) - inverse	1.59	3.07	-1.24		3.01	-6.80	0.30	-5.89		8.70	22.38	38.16	22.14	49.94	0.69	50.26
(D) - inverse	2.92		8.47				0.28	0.91		12.33		35.82			0.67	2.19

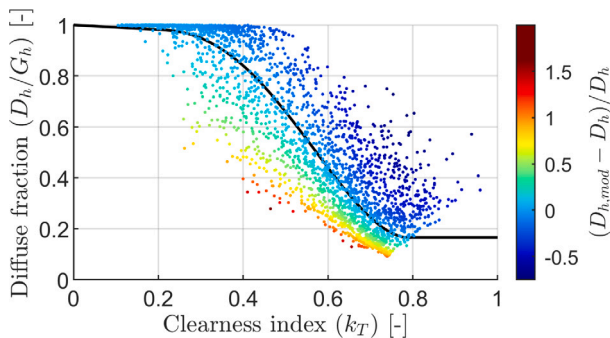


Fig. 12. Diffuse fraction vs. clearness index for configuration CC #1, case (A). Black line shows Erbs correlation according to Eq. (2). The color bar shows the error ratio. (For interpretation of the references to color in this figure legend, the reader is referred to the web version of this article.)

For low levels of the clearness index, the model performs well, but scattering increases for higher clearness indices.

As suggested by Perez et al. (1987) and others, the additional parameters sky clearness, sky brightness, and zenith angle are used to analyze the data scattering observed in Fig. 12. To eliminate the dependence of the sky clearness on the zenith angle, Perez et al. (1990) provided the following expression, denoted by ϵ' :

$$\epsilon' = \frac{(D_h + I_n)/D_h + 1.041 \theta_z^3}{1 + 1.041 \theta_z^3} \quad (25)$$

The sky brightness is given as:

$$\Delta = \frac{D_h \text{ AM}}{I_{on}} \quad (26)$$

where AM is the air mass calculated with the model of Kasten and Young (1989).

In Fig. 13, the sky brightness vs. sky clearness is shown for the same data set as in Fig. 12. All color bars have identical scaling. Subplot Fig. 13a shows that the model substantially overestimates the diffuse fraction when ϵ' is high. Clear sky conditions (i.e., those with a high clearness index; seen in the bottom right corner of Fig. 12), belong to this category. As sky clearness decreases, the turbidity increases, as does the accuracy of the correlation. For conditions that are categorized as “intermediate skies” (Perez et al., 1987), i.e., those with a further decrease in sky clearness and high sky brightness, the correlation underestimates the diffuse horizontal fraction. For sky clearness indices close to 1, where dark and bright overcast skies belong, the correlation is accurate. Similar findings were reported by Padovan and Del Col (2010). Thus, the Erbs correlation tends to overestimate the diffuse fraction in spring and summer due to the prevailing clear sky conditions (Erbs et al., 1982). However, this is always climate-dependent. Although only experimental data from spring and summer were used, the diffuse fraction for the radiation experiments was still underestimated due to the fluctuating local weather conditions that were often characterized by intermediate sky conditions.

The observed pattern for the horizontal is transposed to the tilted plane, as shown in the bottom subplot, Fig. 13b, making it clear that the model bias strongly correlates with sky conditions. Similarly, errors of the diffuse irradiance prediction for the horizontal and tilted planes are strongly correlated, as shown in Fig. 14.

For cases (A) and (C), the substitution of the Erbs model by another separation model will affect the output of the Hay-C model. Choosing an optimal separation model is difficult, as model performances are climate-dependent and vary with the time-scale (Blaga, 2019). Most separation models have been developed for hourly values

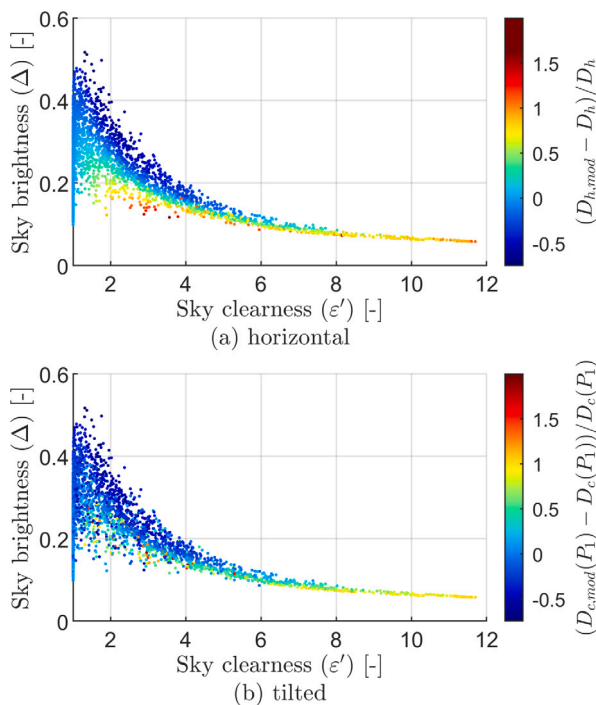


Fig. 13. Sky brightness vs. sky clearness for configuration CC #1, case (A) showing (a) diffuse horizontal and (b) diffuse tilted irradiance. Color bars show error ratio with the same scale as in Fig. 12. (For interpretation of the references to color in this figure legend, the reader is referred to the web version of this article.)

and only recently, models on minute-levels have been proposed. A promising candidate for 1-min resolution is the *Engerer2* model (Bright and Engerer, 2019) as shown in a validation study by Gueymard and Ruiz-Arias (2016). For case (A), the use of alternative separation models in the modeling process (see Fig. 3) is straightforward, as the direct and diffuse irradiance components, I_h and D_h , can simply be replaced by the output of another separation model. For case (D), it is more difficult, as invertibility problems might occur, especially if the relationship between clearness index and diffuse fraction is non-injective (Ridley et al., 2010), as it is the case for *Engerer2*. Further studies should systematically compare the performance of separation models in connection with the *Hay-C* model.

4.4. Model performance analysis for radiation distribution

The accuracy of the model prediction for sensors P_2 to P_5 is shown in Fig. 15 for all configurations, case (D). The model follows the distinct shape of the diffuse irradiance distribution along the collector height. The modeled irradiance for P_2 is close to P_1 , as is the measured irradiance, accounting for the obstructed horizon toward the south. For the wide row spacing (CC #3-6), the model predicts the atypical behavior of slightly higher irradiance values for P_3 than P_1 . This modeling feature is due to the fact, that view factors from the collector towards the sky decrease along the collector height from top to bottom, whereas view factors towards the ground (and typically backside) segments increase. Higher irradiance levels at lower positions occur if increased reflections overcompensate for the reduced sky view, but this effect is typically small.

The prediction accuracy for the sensors closer to the top sensor is significantly higher than for sensor P_5 , where the model still substantially overestimates the diffuse irradiance for the narrow row spacings (CC #1-3). However, the diffuse irradiance prediction for the narrow row spacings is remarkably better than assuming the diffuse irradiance to be constant along the collector height, which is the

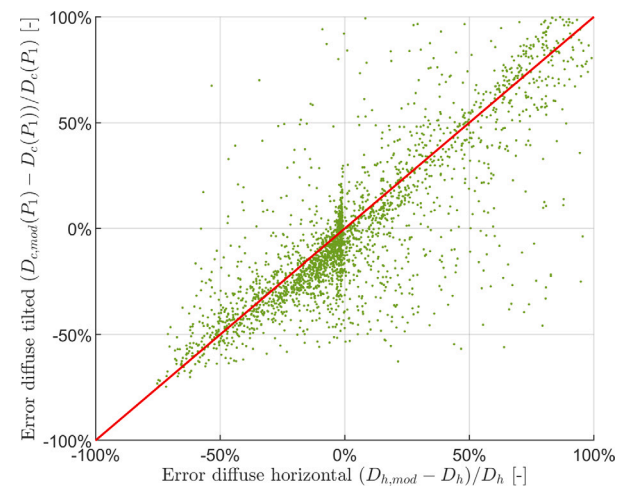


Fig. 14. Error of diffuse horizontal vs. transposed diffuse tilted irradiance for configuration CC #1, case (A). Red line indicates a linear mapping of %MBE. (For interpretation of the references to color in this figure legend, the reader is referred to the web version of this article.)

case for traditional transposition models. The reduction of the global tilted irradiance is less extreme, as all sensors receive the same direct irradiance (no shading), following the same pattern regarding model deviations.

A probable reason for the overestimation of the diffuse irradiance towards the bottom of the collector is the partial blocking of the circumsolar diffuse radiation when the sun is very close to shading objects. Fig. 16 shows the model bias in relation to the angular distance of the sun altitude to the shading line for the bottom sensor, P_5 , configuration CC #1, case (D). The bias is clearly reduced as the angular distance from the shading line increases. Conditions close to the shading line are sensitive to assumptions on the distribution of the circumsolar radiation and the geometric parameters describing the collector array. Note that for the model validation, only data with no shading has been selected. For these conditions, the model assumes that the full circumsolar radiation is received by the collector, leading to an overestimation. However, for simulations where conditions with shading are also considered, the circumsolar irradiance will be underestimated for shaded conditions, resulting in a (partial) compensation of errors.

4.5. Comparison to the original Hay model

A comparative performance analysis of the original Hay model and the *Hay-C* model is shown in Fig. 17. For all configurations, the bias of the original Hay model is more positive relative to the *Hay-C* model. The original Hay model consistently overestimates the irradiance levels as view obstructions are not accounted for. The bias is substantially higher for the narrow row spacings (CC #1-3), where view obstructions have a larger impact. For these configurations, the *Hay-C* model outperforms the original Hay model by around 4%. For the wider row spacings (CC #4-6), the model performances are similar, as view obstructions only have a minor effect and the average global tilted irradiance is nearly uniform along the collector height.

5. Conclusion

The impact of view obstructions on the incident diffuse irradiance on panels and solar collectors installed in fixed-tilted arrays was analyzed experimentally for six array configurations and a novel anisotropic transposition model, called *Hay-C* model, was developed. The following conclusions may be drawn:

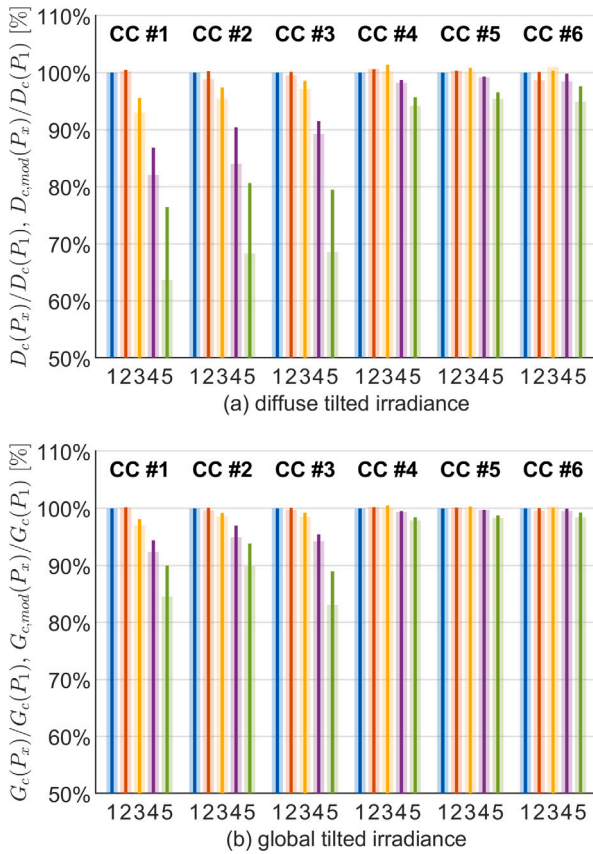


Fig. 15. Comparison of modeled and measured irradiance along the collector height for all collector configurations for the inverse direction (case (D)). Dark, thin bars are predicted values with the Hay-C model. Semi-transparent, thick bars are measured values (also shown in Fig. 10). Distributions for (a) diffuse irradiance and (b) global irradiance are relative to the top sensor ($P_1 = 100\%$). Numbers 1 to 5 refer to sensors P_1 to P_5 .

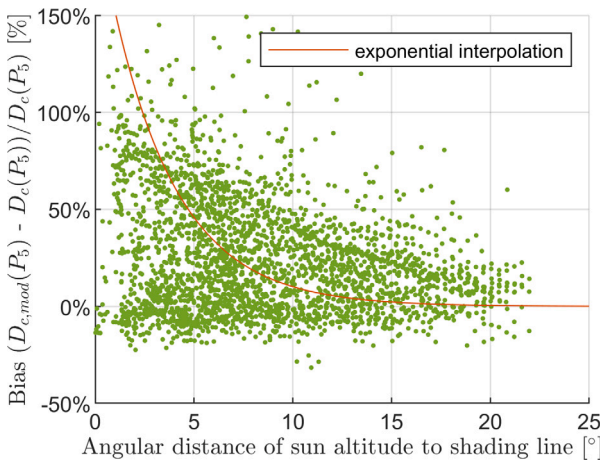


Fig. 16. Model bias vs. angular distance to shading line for configuration CC #1, case (D). The angular distance is defined as the angle between the vector pointing upwards to the sun from sensor P_3 and the vector pointing to the top edge of the front collector row with the same azimuth (the front collector row was relevant for shading for sensor P_5 in configuration CC #1, as the angular distance to the obstructed horizon was greater).

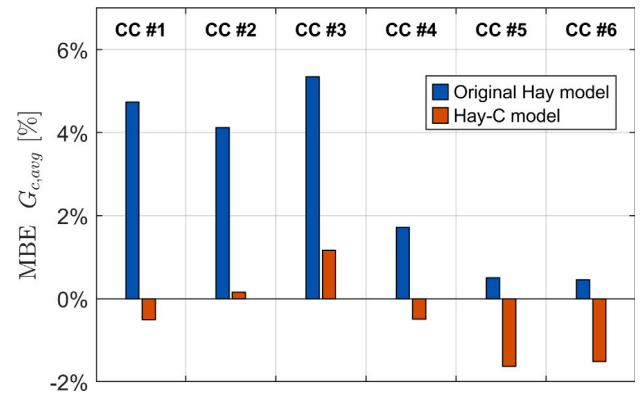


Fig. 17. Comparison of original Hay model and Hay-C model for average global tilted irradiance $G_{c,avg}$. The original Hay model predicts uniform values along the collector height. The predicted global tilted irradiance of the Hay model is therefore used to calculate %MBE for average global tilted irradiance.

1. Typically, the diffuse irradiance decreases monotonically along the collector height from top to bottom. As an exception, diffuse irradiance levels at the midpoint of the collector were slightly higher than at the top for the wide row spacing (6 m), as increased reflections towards the bottom of the collector overcompensated the sky view obstructions.

2. The impact of view obstructions strongly depends on the field layout and is important to consider for narrow row spacings and steep collector tilt angles. The most extreme effects were documented for the configuration with 3.5 m row spacing and 45° tilt angle (1.67 relative row spacing), where the average diffuse irradiance was reduced by 11%, relative to the top of the collector. In contrast, for the configurations with 6 m row spacing, the average diffuse irradiance was reduced only by 1%–2%.

3. The Hay-C model is able to accurately capture the distinct shape of the non-uniform diffuse irradiance distribution along the collector height. For a total of 24 analyzed scenarios, relative mean bias errors for the average diffuse tilted irradiance were below $\pm 1\%$ for 5 scenarios, between $\pm 1\%$ –7% for 13 scenarios and $\pm 8\%$ –14% for 6 scenarios.

4. The combination of the Hay-C model with the Erbs separation model reveals a dependency of the prediction error on the sky conditions, where the diffuse tilted irradiance is underestimated for clear skies and overestimated for intermediate skies with high sky brightness.

5. Very close proximity of the sun to the shading line results in a higher model bias, as these conditions are very sensitive to assumptions of the circumsolar radiation and the geometric parameters describing the collector array.

6. The inverse application of the Hay-C model, i.e. obtaining global horizontal from global tilted irradiance, allows an accurate estimation of the horizontal irradiance. Modeling errors for the inverse direction are similar in magnitude to the forward direction, but opposite in sign.

These results imply, that relying on irradiance measurements from the top of the collector, as is common practice for solar plants, leads to a substantial overestimation of the average diffuse tilted irradiance for narrow row spacings. Subsequently, conversion efficiencies and performance ratios of solar plants can be misleading. The Hay-C model allows to correct this effect for an improved performance assessment. The model also provides accurate irradiance predictions for the optimal design of fixed-tilt arrays, analysis of non-uniform diffuse irradiance patterns (e.g. for current mismatch in PV panels) and calculation of local global horizontal irradiance (e.g. for power forecasting).

$$\begin{aligned}
 \underbrace{\begin{bmatrix} G_{c,1} \\ \vdots \\ G_{c,m} \\ G_{u,1} \\ \vdots \\ G_{u,p} \\ G_{v,1} \\ \vdots \\ G_{v,q} \end{bmatrix}}_{\vec{G}_{inc}} &= \underbrace{\begin{bmatrix} 1 & \cdots & 0 & -\rho_{u,1}F_{c,1 \rightarrow u,1} & \cdots & -\rho_{u,p}F_{c,1 \rightarrow u,p} & -\rho_{v,1}F_{c,1 \rightarrow v,1} & \cdots & -\rho_{v,q}F_{c,1 \rightarrow v,q} \\ \vdots & \ddots & \vdots & \vdots & \vdots & \vdots & \vdots & \vdots & \vdots \\ 0 & \cdots & 1 & -\rho_{u,1}F_{c,m \rightarrow u,1} & \cdots & -\rho_{u,p}F_{c,m \rightarrow u,p} & -\rho_{v,1}F_{c,m \rightarrow v,1} & \cdots & -\rho_{v,q}F_{c,m \rightarrow v,q} \\ -\rho_{c,1}F_{u,1 \rightarrow c,1} & \cdots & -\rho_{c,m}F_{u,1 \rightarrow c,m} & 1 & \cdots & 0 & -\rho_{v,1}F_{u,1 \rightarrow v,1} & \cdots & -\rho_{v,q}F_{u,1 \rightarrow v,q} \\ \vdots & \ddots & \vdots & \vdots & \ddots & \vdots & \vdots & \ddots & \vdots \\ -\rho_{c,1}F_{u,p \rightarrow c,1} & \cdots & -\rho_{c,m}F_{u,p \rightarrow c,m} & 0 & \cdots & 1 & -\rho_{v,1}F_{u,p \rightarrow v,1} & \cdots & -\rho_{v,q}F_{u,p \rightarrow v,q} \\ -\rho_{c,1}F_{v,1 \rightarrow c,1} & \cdots & -\rho_{c,m}F_{v,1 \rightarrow c,m} & -\rho_{u,1}F_{v,1 \rightarrow u,1} & \cdots & -\rho_{u,p}F_{v,1 \rightarrow u,p} & 1 & \cdots & 0 \\ \vdots & \ddots & \vdots & \vdots & \ddots & \vdots & \vdots & \ddots & \vdots \\ -\rho_{c,1}F_{v,q \rightarrow c,1} & \cdots & -\rho_{c,m}F_{v,q \rightarrow c,m} & -\rho_{u,1}F_{v,q \rightarrow u,1} & \cdots & -\rho_{u,p}F_{v,q \rightarrow u,p} & 0 & \cdots & 1 \end{bmatrix}}_{(I - FR)^{-1}} \cdot \underbrace{\begin{bmatrix} I_{c,1} + D_{s,1} \\ \vdots \\ I_{c,m} + D_{s,m} \\ I_{u,1} + D_{s,u,1} \\ \vdots \\ I_{u,p} + D_{s,u,p} \\ I_{v,1} + D_{s,v,1} \\ \vdots \\ I_{v,q} + D_{s,v,q} \end{bmatrix}}_{(\vec{I} + \vec{D})} \quad (A.1)
 \end{aligned}$$

Box I.

CRedit authorship contribution statement

Daniel Tschopp: Developed the concept of this paper, Wrote the original draft, Developed the *Hay-C* model, Validated the model with measurement data, Performed the simulations. **Adam R. Jensen:** Developed the concept of this paper, Wrote the original draft, Conducted the in situ measurements, Processed and analyzed measurement data, Supported the model development. **Janne Dragsted:** Conceptualized the radiation measurement setup, Supervised the measurement campaign. **Philip Ohnewein:** Supported the model development and implementation. **Simon Furbo:** Conceptualized the radiation measurement setup, Supervised the measurement campaign.

Declaration of competing interest

The authors declare that they have no known competing financial interests or personal relationships that could have appeared to influence the work reported in this paper.

Data availability

Measurement data from the DTU Climate Station, including additional basic weather parameters, are freely available online at <http://climatestationdata.byg.dtu.dk>.

Acknowledgments

The authors would like to express their gratitude to the following people for valuable contributions to this paper: Bengt Perers (DTU), Robert Hausner (AEE INTEC), Christoph Rohringer (AEE INTEC), Alexander Thür (University of Innsbruck), and Wolfgang Streicher (University of Innsbruck). This work was supported by the Danish Energy Agency, Denmark, Energy Technology Development and Demonstration Program (EUDP), grant no. 64017-05163; and the Austrian Research Promotion Agency, PhD scholarship project CollFieldEff⁺, grant no. FFG 854735. Also, the research work contributes to IEA SHC Task 55 – *Towards the Integration of Large SHC Systems into District Heating and Cooling (DHC) Networks* and IEA PVPS Task 16 – *Solar Resource for High Penetration and Large Scale Applications*.

Appendix A. Radiation exchange between collector, ground, and backside segments

The explicit form of Eq. (20) is given by (A.1) in Box I for m collector segments, p ground segments, and q backside segments. \vec{G}_{inc} is a $(m + p + q) \times 1$ vector containing the global irradiance (received from the sky and reflections) on the collector, $G_{c,1 \dots m}$, ground, $G_{u,1 \dots p}$, and backside, $G_{v,1 \dots q}$. $\vec{I} + \vec{D}$ denote the sum of the direct and diffuse irradiance from the sky. Note that the view factors among the collector,

ground, and backside segments are zero, because they are positioned in one plane respectively. By default, reflectance coefficients of the collector segments are set to zero. If all reflectance coefficients are set to zero, the expression $(I - FR)^{-1}$ becomes the identity matrix I , implying $\vec{G}_{inc} = \vec{I} + \vec{D}$. If at least one reflectance coefficient > 0 , then $\vec{G}_{inc} > \vec{I} + \vec{D}$. For the chosen settings in the paper, the calculation of $(I - FR)^{-1}$ was numerically stable, for nearly singular matrices a numerically stable procedure, e.g. singular value decomposition, is recommended (Klema and Laub, 1980).

Appendix B. Supplementary data

Supplementary material related to this article can be found online at <https://doi.org/10.1016/j.solener.2021.10.083>.

References

- Andersen, E., Johansen, Jakob Berg, Furbo, Simon, Perers, Bengt, Andersen, Lars Kokholm, Dragsted, Janne, Dannemand, Mark, 2017. Availability of high quality weather data measurements. DTU Byg Repor R-379, Department of Civil Engineering, Technical University of Denmark.
- Anoma, M.A., Jacob, D., Bourne, B.C., Scholl, J.A., Riley, D.M., Hansen, C.W., 2017. View factor model and validation for bifacial PV and diffuse shade on single-axis trackers. In: 2017 IEEE 44th Photovoltaic Specialist Conference (PVSC). IEEE, Washington, DC, pp. 1549–1554. <http://dx.doi.org/10.1109/PVSC.2017.8366704>.
- Appelbaum, J., 2018. The role of view factors in solar photovoltaic fields. *Renew. Sustain. Energy Rev.* 81, 161–171. <http://dx.doi.org/10.1016/j.rser.2017.07.026>.
- Appelbaum, J., Bany, J., 1979. Shadow effect of adjacent solar collectors in large scale systems. *Sol. Energy* 23 (6), 497–507. [http://dx.doi.org/10.1016/0038-092X\(79\)90073-2](http://dx.doi.org/10.1016/0038-092X(79)90073-2).
- Appelbaum, J., Massalha, Y., Aronescu, A., 2019. Corrections to anisotropic diffuse radiation model. *Sol. Energy* 193, 523–528. <http://dx.doi.org/10.1016/j.solener.2019.09.090>.
- Ayieko, C.O., Musembi, R.J., Ogacho, A.A., Aduda, B.O., Muthoka, B.M., Jain, P.K., 2015. Controlled texturing of aluminum sheet for solar energy applications. *Adv. Mater. Phys. Chem.* 05 (11), 458–466. <http://dx.doi.org/10.4236/ampc.2015.511046>.
- Bany, J., Appelbaum, J., 1987. The effect of shading on the design of a field of solar collectors. *Sol. Cells* 20 (3), 201–228. [http://dx.doi.org/10.1016/0379-6787\(87\)90029-9](http://dx.doi.org/10.1016/0379-6787(87)90029-9).
- Bava, F., Furbo, S., 2018. Impact of different improvement measures on the thermal performance of a solar collector field for district heating. *Energy* 144, 816–825. <http://dx.doi.org/10.1016/j.energy.2017.12.025>.
- Blaga, R., 2019. The impact of temporal smoothing on the accuracy of separation models. *Sol. Energy* 191, 371–381. <http://dx.doi.org/10.1016/j.solener.2019.08.078>.
- Blanc, P., Espinar, B., Geuder, N., Gueymard, C., Meyer, R., Pitz-Paal, R., Reinhardt, B., Renné, D., Sengupta, M., Wald, L., Wilbert, S., 2014. Direct normal irradiance related definitions and applications: The circumsolar issue. *Sol. Energy* 110, 561–577. <http://dx.doi.org/10.1016/j.solener.2014.10.001>.
- Bright, J., Engerer, N., 2019. Engerer2: global re-parameterisation, update, and validation of an irradiance separation model at different temporal resolutions. *Journal of Renewable and Sustainable Energy* 11 (3), 033701. <http://dx.doi.org/10.1063/1.5097014>.

- Celik, A.N., Muneer, T., 2013. Neural network based method for conversion of solar radiation data. *Energy Convers. Manage.* 67, 117–124. <http://dx.doi.org/10.1016/j.enconman.2012.11.010>.
- De Simón-Martín, M., Alonso-Tristán, C., Díez-Mediavilla, M., 2017. Diffuse solar irradiance estimation on building's Façades: Review, classification and benchmarking of 30 models under all sky conditions. *Renew. Sustain. Energy Rev.* 77, 783–802. <http://dx.doi.org/10.1016/j.rser.2017.04.034>.
- Duffie, J.A., Beckman, W.A., Blair, N., 2020. *Solar Engineering of Thermal Processes, Photovoltaics and Wind*. John Wiley & Sons.
- Erbs, D.G., Klein, S.A., Duffie, J.A., 1982. Estimation of the diffuse radiation fraction for hourly, daily and monthly-average global radiation. *Sol. Energy* 28 (4), 293–302. [http://dx.doi.org/10.1016/0038-092X\(82\)90302-4](http://dx.doi.org/10.1016/0038-092X(82)90302-4).
- Gu, W., Ma, T., Ahmed, S., Zhang, Y., Peng, J., 2020. A comprehensive review and outlook of bifacial photovoltaic (BPV) technology. *Energy Convers. Manage.* 223, 113283. <http://dx.doi.org/10.1016/j.enconman.2020.113283>.
- Gueymard, C.A., 2009. Direct and indirect uncertainties in the prediction of tilted irradiance for solar engineering applications. *Sol. Energy* 83 (3), 432–444. <http://dx.doi.org/10.1016/j.solener.2008.11.004>.
- Gueymard, C.A., 2014. A review of validation methodologies and statistical performance indicators for modeled solar radiation data: Towards a better bankability of solar projects. *Renew. Sustain. Energy Rev.* 39, 1024–1034. <http://dx.doi.org/10.1016/j.rser.2014.07.117>.
- Gueymard, C.A., Lara-Fanego, V., Sengupta, M., Xie, Y., 2019. Surface albedo and reflectance: Review of definitions, angular and spectral effects, and intercomparison of major data sources in support of advanced solar irradiance modeling over the Americas. *Sol. Energy* 182, 194–212. <http://dx.doi.org/10.1016/j.solener.2019.02.040>.
- Gueymard, C.A., Myers, D.R., 2008. Validation and ranking methodologies for solar radiation models. In: Badescu, V. (Ed.), *Modeling Solar Radiation At The Earth's Surface*. Springer Berlin Heidelberg, Berlin, Heidelberg, pp. 479–510.
- Gueymard, C.A., Myers, D.R., 2009. Evaluation of conventional and high-performance routine solar radiation measurements for improved solar resource, climatological trends, and radiative modeling. *Sol. Energy* 83, 171–185. <http://dx.doi.org/10.1016/j.solener.2008.07.015>.
- Gueymard, C.A., Ruiz-Arias, J.A., 2016. Extensive worldwide validation and climate sensitivity analysis of direct irradiance predictions from 1-min global irradiance. *Sol. Energy* 128, 1–30. <http://dx.doi.org/10.1016/j.solener.2015.10.010>.
- Hay, J.E., Davies, J., 1980. Calculation of the solar irradiance incident on an inclined surface. In: Hay, J.E., Won, T.K. (Eds.), *Proceedings: First Canadian Solar Radiation Data Workshop: April 17–19, 1978*, Toronto, Ontario, Canada. pp. 59–72.
- Hottel, H., Sarofim, A., 1967. *Radiative Transfer*. McGraw-Hill, New York.
- Housmans, C., Bertrand, C., 2017. Evaluation of various procedures transposing global tilted irradiance to horizontal surface irradiance. *Adv. Sci. Res.* 14, 17–22. <http://dx.doi.org/10.5194/asr-14-17-2017>.
- Ivanova, S.M., Gueymard, C.A., 2019. Simulation and applications of cumulative anisotropic sky radiance patterns. *Sol. Energy* 178, 278–294. <http://dx.doi.org/10.1016/j.solener.2018.12.026>.
- Joint Committee for Guides in Metrology, 2008. Evaluation of measurement data – guide to the expression of uncertainty in measurement. In: Bureau International Des Poids Et Mesures.
- Kasten, F., Young, A.T., 1989. Revised optical air mass tables and approximation formula. *Appl. Opt.* 28 (22), 4735. <http://dx.doi.org/10.1364/AO.28.004735>.
- Kipp & Zonen, 2016. *Instruction manual CMP series pyranometer*.
- Kipp & Zonen, 2019. *Datasheet for CHP1 and SHP1 pyrhemometers*.
- Klein, S.A., Beckman, W., Mitchell, J., Duffie, J.A., Duffie, N., Freeman, T., Mitchell, J., Braun, J., Evans, B., Kummer, J., Urban, R., Fiskel, A., Thornton, J., Blair, N., Williams, P., Bradley, P., McDowell, T., Kummert, M., Arias, D., Duffie, M., 2009. TRNSYS 17 - a TRAnsient SYstem Simulation Program - Volume 4 Mathematical Reference. Solar Energy Laboratory, University of Wisconsin-Madison, Wisconsin-Madison.
- Klema, V., Laub, A., 1980. The singular value decomposition: Its computation and some applications. *IEEE Trans. Automat. Control* 25 (2), 164–176. <http://dx.doi.org/10.1109/TAC.1980.1102314>.
- Klucher, T., 1979. Evaluation of models to predict insolation on tilted surfaces. *Sol. Energy* 23 (2), 111–114. [http://dx.doi.org/10.1016/0038-092X\(79\)90110-5](http://dx.doi.org/10.1016/0038-092X(79)90110-5).
- Laursen, E.V., Thomsen, R.S., Cappelen, J., 1999. Observed air temperature, humidity, pressure, cloud cover and weather in Denmark: With climatological standard normals 1961–90. Technical Report, Danish Meteorological Institute, Copenhagen.
- Liu, B.Y., Jordan, R.C., 1963. The long-term average performance of flat-plate solar-energy collectors. *Sol. Energy* 7 (2), 53–74. [http://dx.doi.org/10.1016/0038-092X\(63\)90006-9](http://dx.doi.org/10.1016/0038-092X(63)90006-9).
- Long, C., Dutton, E., 2010. *BSRN Global network recommended QC tests, V2.0*.
- Maor, T., Appelbaum, J., 2012. View factors of photovoltaic collector systems. *Sol. Energy* 86 (6), 1701–1708. <http://dx.doi.org/10.1016/j.solener.2012.03.017>.
- Massalha, Y., Appelbaum, J., 2020. Experimental verification of the sky view factor model in multiple-row photovoltaic fields. *J. Sol. Energy Eng.* 142 (2), 5. <http://dx.doi.org/10.1115/1.4044979>.
- Noorian, A.M., Moradi, I., Kamali, G.A., 2008. Evaluation of 12 models to estimate hourly diffuse irradiation on inclined surfaces. *Renew. Energy* 33 (6), 1406–1412. <http://dx.doi.org/10.1016/j.renene.2007.06.027>.
- Ohnweine, P., Tschopp, D., Hamilton-Jones, M., Schrammel, H., 2017. ADA advanced data analysis. AEE INTEC.
- Ohnweine, P., Tschopp, D., Hausner, R., Doll, W., 2020. Dynamic collector array test (D-CAT). Final Report FFG Project 848766 - MeQuSo. Development of methods for quality assessment of large-scale solar thermal plants under real operating conditions. Technical Report, AEE - Institute for Sustainable Technologies, Gleisdorf, Available Online: <https://www.aee-intec.at/Uploads/dateien1538.pdf>.
- Padovan, A., Del Col, D., 2010. Measurement and modeling of solar irradiance components on horizontal and tilted planes. *Sol. Energy* 84 (12), 2068–2084. <http://dx.doi.org/10.1016/j.solener.2010.09.009>.
- Perez, R., Ineichen, P., Seals, R., Michalsky, J., Stewart, R., 1990. Modeling daylight availability and irradiance components from direct and global irradiance. *Sol. Energy* 44 (5), 271–289. [http://dx.doi.org/10.1016/0038-092X\(90\)90055-H](http://dx.doi.org/10.1016/0038-092X(90)90055-H).
- Perez, R., Seals, R., Ineichen, P., Stewart, R., Menicucci, D., 1987. A new simplified version of the Perez diffuse irradiance model for tilted surfaces. *Sol. Energy* 39 (3), 221–231. [http://dx.doi.org/10.1016/S0038-092X\(87\)80031-2](http://dx.doi.org/10.1016/S0038-092X(87)80031-2).
- Perez, R., Stewart, R., Arbogast, C., Seals, R., Scott, J., 1986. An anisotropic hourly diffuse radiation model for sloping surfaces: Description, performance validation, site dependency evaluation. *Sol. Energy* 36 (6), 481–497. [http://dx.doi.org/10.1016/0038-092X\(86\)90013-7](http://dx.doi.org/10.1016/0038-092X(86)90013-7).
- Reindl, D.T., Beckman, W.A., Duffie, J.A., 1990. Evaluation of hourly tilted surface radiation models. *Sol. Energy* 45 (1), 9–17. [http://dx.doi.org/10.1016/0038-092X\(90\)90061-G](http://dx.doi.org/10.1016/0038-092X(90)90061-G).
- Ridley, B., Bolland, J., Lauret, P., 2010. Modelling of diffuse solar fraction with multiple predictors. *Renew. Energy* 35 (2), 478–483. <http://dx.doi.org/10.1016/j.renene.2009.07.018>.
- Robinson, D., Stone, A., 2004. Solar radiation modelling in the urban context. *Sol. Energy* 77 (3), 295–309. <http://dx.doi.org/10.1016/j.solener.2004.05.010>.
- Saint-Drenan, Y.-M., Barbier, T., 2019. Data-analysis and modelling of the effect of inter-row shading on the power production of photovoltaic plants. *Sol. Energy* 184, 127–147. <http://dx.doi.org/10.1016/j.solener.2019.03.086>.
- Sartorius, S., 2020. Bisection method root finding. <https://github.com/sky-s/bisection>, GitHub, downloaded 2020-03-27.
- Sobri, S., Koohi-Kamali, S., Rahim, N.A., 2018. Solar photovoltaic generation forecasting methods: A review. *Energy Convers. Manage.* 156, 459–497. <http://dx.doi.org/10.1016/j.enconman.2017.11.019>.
- Tschopp, D., Tian, Z., Berberich, M., Fan, J., Perers, B., Furbo, S., 2020. Large-scale solar thermal systems in leading countries: A review and comparative study of Denmark, China, Germany and Austria. *Appl. Energy* 270, 114997. <http://dx.doi.org/10.1016/j.apenergy.2020.114997>.
- Varga, N., Mayer, M.J., 2021. Model-based analysis of shading losses in ground-mounted photovoltaic power plants. *Sol. Energy* 216, 428–438. <http://dx.doi.org/10.1016/j.solener.2021.01.047>.
- Voyant, C., Nottot, G., Kalogirou, S., Nivet, M.-L., Paoli, C., Motte, F., Fouilloy, A., 2017. Machine learning methods for solar radiation forecasting: A review. *Renew. Energy* 105, 569–582. <http://dx.doi.org/10.1016/j.renene.2016.12.095>.
- World Meteorological Organization, 2017. Guide to meteorological instruments and methods of observation WMO-No. 8: Chapter 7 measurement of radiation. In: *Guide To Meteorological Instruments and Methods of Observation*, seventh ed.
- Yang, D., 2016. Solar radiation on inclined surfaces: Corrections and benchmarks. *Sol. Energy* 136, 288–302. <http://dx.doi.org/10.1016/j.solener.2016.06.062>.
- Yang, D., Dong, Z., Nobre, A., Khoo, Y.S., Jirutitijaroen, P., Walsh, W.M., 2013. Evaluation of transposition and decomposition models for converting global solar irradiance from tilted surface to horizontal in tropical regions. *Sol. Energy* 97, 369–387. <http://dx.doi.org/10.1016/j.solener.2013.08.033>.
- Yang, D., Ye, Z., Nobre, A.M., Du, H., Walsh, W.M., Lim, L.I., Reindl, T., 2014. Bidirectional irradiance transposition based on the Perez model. *Sol. Energy* 110, 768–780. <http://dx.doi.org/10.1016/j.solener.2014.10.006>.